Two-photon polymerization of femtosecond high-order Bessel beams with aberration correction

Erse Jia (贾而穑)[1], Chen Xie (谢 辰)[1]*, Na Xiao(肖 娜)[1], Francois Courvoisier[2] and Minglie Hu(胡明列)[1]

[1]Ultrafast Laser Laboratory, Key Laboratory of Opto-electronic Information Technical Science of Ministry of Education, School of Precision Instruments and Opto-electronics Engineering, Tianjin University, Tianjin 300072, China

[2]FEMTO-ST Institute, Université de Bourgogne-Franche-Comté UMR-6174, 25030 Besançon, France
*Corresponding author: xie_chen@tju.edu.cn

In the femtosecond two-photon polymerization (2PP) experimental system, optical aberrations degrade the fabrication quality. To solve this issue, a multichannel interferometric wave-front sensing technique is adopted in the adaptive laser processing system with a single phase-only spatial light modulator. 2PP fabrications using corrected high-order Bessel beams with the above solution have been conducted and high-quality microstructure arrays of micro-tubes with 20 microns diameter are rapidly manufactured. The effectiveness of the proposed scheme is demonstrated by comparing the beam intensity distributions and 2PP results before and after aberration corrections.
Keywords*:* Femtosecond laser, Two-photon polymerization, Aberration correction, Bessel beams

1. Introduction

Femtosecond two-photon polymerization [1-5] (2PP) is widely used in the fabrication of three-dimensional complex architectures with a sub-micrometer resolution. Recent applications are templates for quantum dots [6], scanning-probe microscopes [7], microchips [8], and biomimetic 4D printing [9]. The conventional 2PP procedures utilize the tightly-focused femtosecond laser beam to trigger polymerization inside the photoresist. In recent years, femtosecond 2PP based on adaptive optics [10-13] has attracted considerable interest due to the enhanced fabrication efficiency with different structured light beams, such as Bessel beams [14], optical vortex beams [15-17], abruptly autofocusing beams [18] and axilens beams with long focal depths [19]. Within these procedures, the spatial light modulators (SLM) are introduced to generate arbitrary optical patterns through computer generated hologram (CGH) algorithm [20] so that various structures could be fabricated via one-step exposure. In fact, many factors in the 2PP setup combining the ultrafast laser and the adaptive optics can introduce undesired aberrations, such as the walk-off effect in the nonlinear crystal, the internal stress and the nonlinear response of the adaptive devices, and the manufacturing defects or assembly errors of the optical element.

On the other side, Bessel beams are notable for the diffraction-resistance and self-healing behaviors. Besides these properties, high-order Bessel beams also show potentials to synthesize more complex structured lights [21, 22]. Based on the above characteristics, high-order Bessel beams have been widely used in micro-nano manufacturing [23], biological imaging [24], optical tweezers [25], optical communication [26, 27] and other fields. However, the aberrations in the setup significantly affect the application of high-order Bessel beams since their patterns are extremely sensitive to aberrations [28].

Numerous methods can assist in shaping beams and/or removing aberrations in the optical system [29-34], and the SLMs are the critical devices in these adaptive methods. Crucially, these solutions all require relatively advanced mathematical tools, such as the Zernike polynomial, the Gerchberg-Saxton or more complex algorithms. In the application of waveguide writing, the SLM has shown great power in correcting the spherical aberration inside bulky glass [34] and controlling the nonlinear propagation [34, 35]. Despite of the negligible nonlinear propagating effect in the application of 2PP, the SLMs are also playing critical roles by building fabricating systems based on adaptive optics. In such systems, a relay optics system is installed after the SLM to generate micron-scaled structured beams. Further filterings are usually introduced to eliminate the undesired diffracting sub-beams resulting from the superimposed grating phases. Therefore, considering the increased complexity of these systems caused by the pixelated SLM, the above aberration correction approaches will no longer be applicable.

In this paper, we demonstrate the power of aberration correction in our 2PP experimental system based on the multi-channel interferometric wave-front sensing technique. This method was originally developed to restore the intensity distribution of the structured beams in situ [36] requiring no complex mathematical tools. A single phase-only SLM is sufficient to implement this method into optimizing the 2PP system, sparing the heavy work of alignments in installing the system. We verify the effectiveness of this method by comparing the intensity profiles of the high-order Bessel beam before and after the correction. The experimental results of our aberration-free structured beam present excellent agreement with the simulations in the ideal case. With the help of this method, we finally realize the rapid fabrication of high-quality micro-tube structures by directly exposing the high-order Bessel beams into the negative photoresist.

2. Principle of the Aberration Correction

Any given optical field propagating through an optical system can be expressed as a composition of modes in any orthogonal representation [36]. The optimal focusing is achieved if and only if all the modes present the identical phase, which means the strength of constructive interference would be highest between these modes. Therefore, the optimal focusing generally requires accurately compensating the phase of each mode for any beam in the physical setup with imperfect optics. As an adaptive programmable device, the liquid crystal-based SLM can perform versatile tasks, including structured lights generation and optical field detection and/or correction. In our setup, we divide the two-dimensional pixel array on the SLM into M*N channels with equal size. Each channel is filled with blazed grating phase with independent on-off switch, as shown in Fig. 1(a) and (b). With the blazed grating phase, the modulating information in each channel is coded in the first-order diffracting light and spatially separated from the undesired zero-order light. In the procedure of the wave-front sensing, we firstly select a channel as the phase reference and keep this channel on. Then, all the other test channels are successively switched on along the direction shown in Fig. 1(b). The intensity signal in the focal plane of the lens are collected while increasing the phase of the tested channel from 0 to 2π. For the convenience, the amplitude and phase of the i-th test channel and reference channel are respectively denoted by $|U_i|$, φ_i and $|U_r|$, φ_r. The interference intensity I of the first order of diffraction would follow the relation:

$$I \propto |U_i|^2 + |U_r|^2 + 2|U_i||U_r|\cos(\varphi_i - \varphi_r) \qquad (1)$$

Therefore, the phase of the test channel φ_i will be identical with the reference φ_r when the signal tends to reach the maximum. Note that the phase terms in Eq.(1) represent the phase profiles in each channel, which is assumed as nearly homogeneous across the corresponding sub-regional wavefront. After probing all the test channels, the full wave-front would be plotted and a complementary phase map would be readily loaded on the SLM [Fig.1(c)] to achieve aberration compensation. A specific example of correction is shown in Fig.1(c)-(e), with details explained in the following section.

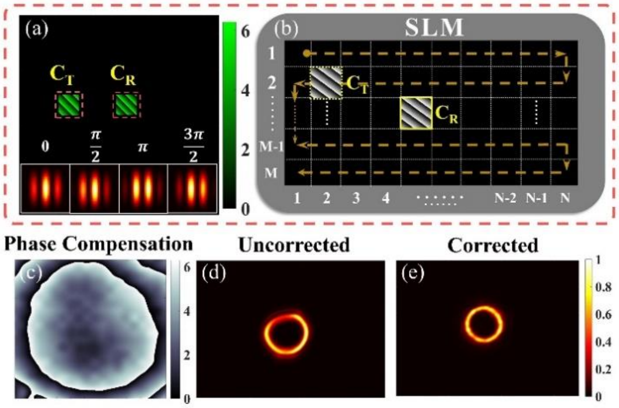

Fig. 1. Schematics of the wave-front sensing. (a) two channels on the SLM, C_T: test channel, C_R: reference channel; insets in (a) show the simulated interference patterns with various phase differences between the test and the reference channels: 0, π/2, π and 3π/2. (b) SLM area division and scanning path of the test channel; (c) the aberration correction mask loaded on the SLM; Fourier spectral profiles of the high-order Bessel beams (d) before and (e) after the correction.

3. Experiments and Result

3.1. Setup

The above aberration detection scheme could be readily integrated in our setup for 2PP as shown in Fig. 2. The laser source is a home-made femtosecond fiber laser amplifying system with standard double-cladding fibers similar to that in [37], enabling 90-fs transform-limited laser pulses centered at 1038 nm output at 1-MHz repetition rate. A BBO crystal is inserted to generate the second harmonic (SH) wave for the 2PP fabricating process. Considering the damage threshold of the coating on the crystal surface, the fabrication does not require the femtosecond laser to work at full load. After expansion, the SH wave of a diameter ~ 8 mm illuminates the phase-only SLM (Holoeye PLUTO, 1920x1080 pixels) with the exposed power adjusted by the neutral density (ND) filter. The telescope composed by the lens (f=1m) and the microscope objective (Olympus 20×, NA=0.4) shrinks the modulated waves into the micro-scaled patterns. A mechanical shutter is used to control the exposure time in the sample. The CCD camera is located at the focal plane of the lens to perform the wave-front detection.

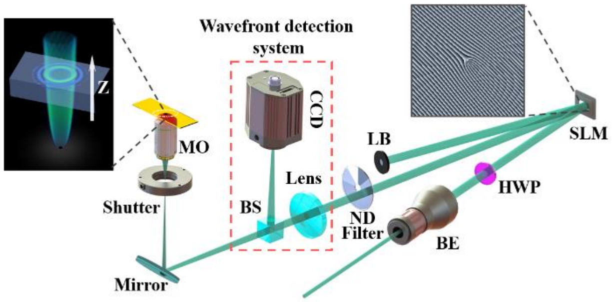

Fig. 2. Schematic of the setup: BE, beam expander; HWP, half-wave plate; SLM, spatial light modulator; LB, laser block; ND filter, neutral density filter; BS, beam splitter; Shutter, mechanical shutter; MO, microscope objective; CCD, CCD camera. Inset close to the SLM presents the phase pattern to generate the Bessel vortex beams; the corresponding 3D light fields at the focus area in the slide are presented in the inset close to MO.

In order to achieve more accurate wave-front detection, the number of divided areas on the SLM is in principle the more the better. However, a single channel with very few pixels would be too problematic to implement, resulting in too weak intensity of the interference patterns to be detected. Since the optical aberration in a typical device is a smooth function with low spatial frequencies, dividing the pixel panel into no less than 10×10 channels can provide sufficient sampling. To ensure the fineness of the detected wave-front, we divided the SLM panel into 20×20 channels in our tests together with π/10 phase increment. After probing the whole panel with the scheme in the previous section, we obtain the compensating phase as shown in Fig. 1(c). We note here that no great effort is made in aligning the beam path, leading to a significant aberration introduced in terms of mis-alignment. It is noteworthy that more than 4π phase fluctuation across the beam are detected, and thus a highly distorted field from the desired pattern would be expected. We remark that a high-quality objective from Olympus is adopted in the current setup to suppress the aberrations after the long focal lens in the telescope. But it is also possible to correct the aberration of the whole optical system with our scheme by inserting another lens after the objective and monitoring the signal in its focal plane. This is not realized in the current setup due to the rather limit space. Further engineering the setup is also part of our future work.

3.2. Aberration correction

As in [38], we apply the phase below on the input beam to generate high-order Bessel beams:

$$\phi(r,\theta) = -k\sin(\gamma)r + m\theta \qquad (2)$$

where k is the wave vector in vacuum, γ is the cone angle between the refracted conical wave and the optical axis and m is the vortex order. In this paper, we take m=6 and γ=4°. Note that a blazed grating phase was also added to the SLM to separate the desired beam from the unmodulated zero-order light [39]. The Fourier spectra of the Bessel beams are further recorded, showing the distorted profile without correction in Fig.1(d). After superimposing the compensating mask, the Fourier spectra is well corrected in terms of both circularity and intensity uniformity [Fig.1(e)]. Besides, a slightly shrunk radius also occurs after the correction, which can be explained by the overall converging property of the compensating phase map.

Fig. 3 presents the longitudinal and transverse intensity profiles of our high-order Bessel beams in direct space after the objective MO in Fig.2. Numeric results of the Bessel beams generated from an ideal Gaussian beam are presented in the first row of Fig. 3 for comparison. The simulations are performed based on angular spectrum method as in our previous studies [38, 40]. The second and third rows show the corresponding intensity profiles in experiments before and after the correction, respectively. After the transitionally expanding region along propagation [38, 40], the main lobe converges to a constant diameter (~20μm) in the non-diffracting regime as shown in Fig.3(g). However, the uncorrected main lobe cannot maintain its non-diffracting feature as shown in Fig.3(b). Meanwhile, the annular intensity profile has also been seriously distorted with less annular rings. As expected, the correction operation has significantly reduced the detrimental aberrations, as shown in Fig. 3(c) and (f). The shape of the central intensity tube returns to the ideal trajectory and the intensity profile also restore its original pattern. Overall, the high-order Bessel beams after aberration correction are highly consistent with the ideal beam in the simulation.

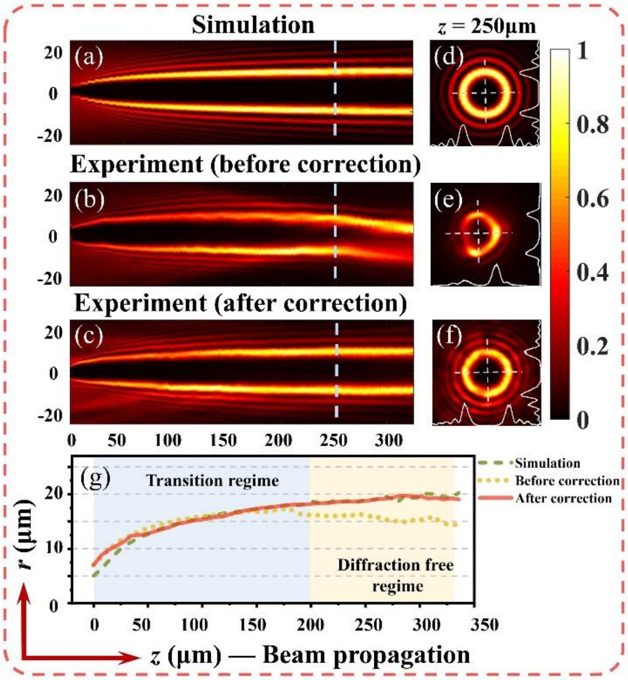

Fig. 3. Correction of the high-order Bessel beams with vortex charge m = 6: the longitudinal intensity profiles along propagation in (a) simulation and in experiments (b) before and (c) after the correction; corresponding transverse intensity profiles at z = 250μm in (d)-(f); (g) the evolution of the main lobe size along the propagation.

3.3. Results and analyses

Encouraged by the high consistency between the restored and the ideal beam profile, we perform the two-photon polymerization as a further test. In the 2PP fabrication, the negative photoresist (MicroChem SU-8 2075, diluted with cyclopentanone, with the ratio of SU-8 : cyclopentanone = 5 : 1) is uniformly spin-coated on the glass slide substrate at 1500rpm. Soft baking was performed on a hot plate for 5 min at 65 °C and then for 10 min at 95 °C. Up to 1.5 mW average power of the ultrafast SH wave is exposed in the prepared sample at 1-MHz repetition rate, corresponding to 1.5nJ single pulse energy. The relatively low repetition rate can well avoid the occurrence of thermal issue in the manufacturing process. Considering the transitionally expanding ring lobe along propagation may occur more significantly for Bessel beams of certain parameters as shown in Fig.3 and discussed in our previous work [38, 40], non-diffracting region should be carefully positioned to cross the whole photoresist layer to guarantee the fabrication of well-shaped micro-tubes as shown in the inset of Fig.2. Once the axial position of the beam is well selected, transversal movement in the horizontal plane together with exposure at proper power level would allow the rapid fabrication of the micro-tube array. The average time to fabricate each single micro-tube, including the movement and the exposure, is no more than 0.8sec without optimization. After the hard baking following the exposure, the photoresist is developed to produce the micro-patterns as high as 30μm as shown in Fig.4.

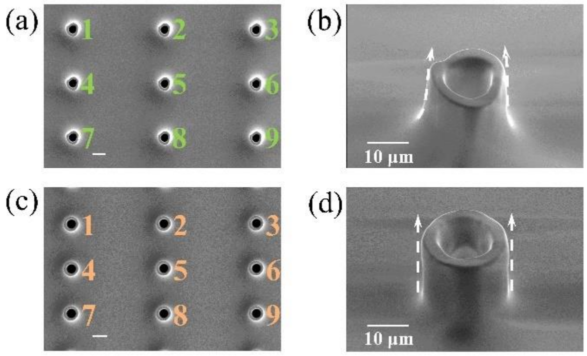

Fig. 4. SEM photos of micro-tube structures fabricated with high-order Bessel beams (a)-(b) before and (c)-(d) after aberration correction; the scaling bars without notation represent 20μm.

The SEM images of the micro-tubes are obtained with ZEISS Gemini 300 electronic microscope as shown in Fig. 4. For comparison, we firstly perform the fabrication of micro-tubes with the uncorrected high-order Bessel beams of vortex charge m=6. It can be seen in Fig.4 (a)-(c) that the micro-tubes are seriously deformed due to the uncorrected Bessel beams in the non-diffraction region as shown in Fig.3. Fig.4 (d)-(f) present the micro-tube arrays with the single units fabricated by aberration-free high-order Bessel beams. It is apparent that the uniformity of the fabricated units is very satisfying. The measured outer ring diameters and wall thickness of the microstructures are ~ 20.8 μm and ~ 4.3 μm respectively.

The white dashed lines with arrows in Fig. 4(c) and (f) outline the outer walls of the micro-tubes before and after the aberration correction. It is noteworthy that the aberration also leads to the tapered wall in Fig. 4(c), i.e. a transitional polymerization region between the glass substrate and the micro-tube bottom. Most importantly, the non-uniform intensity of the uncorrected main lobe would introduce a much higher fluctuation of the local intensity during the 2PP process, which further degrades the inconsistency of the micro-tube wall thickness. Besides, we also found that the micro-tubes with non-uniform shaped walls have higher rates to fall down on the glass substrate. We attribute this to the structural shrinkage induced by the nonuniform light energy deposition along the distorted Bessel beams as shown in Fig.3 [41]. After the phase correction, the above issues are well addressed. Once the high-order Bessel beams are well positioned across the interface between the substrate and the photoresist, no falling-down of the micro-tube structures are observed.

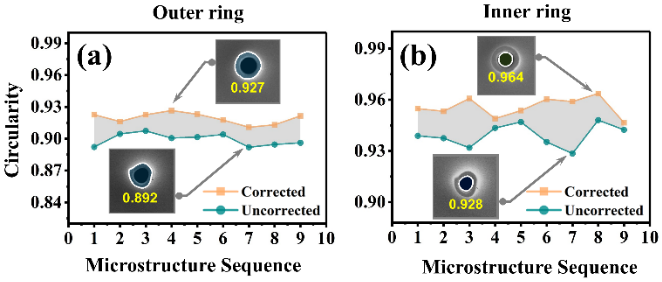

Fig. 5. Circularity measurement results of the micro-tube structures: (a) the outer rings and (b) the inner rings.

In order to quantify the improvement in fabrication quality after the aberration removal, we extract the contours of the inner and outer rings of the microstructures in the SEM photos and measure their circularity. The ring contours are extracted by a combination of conventional operations in digital image processing, such as binarization, smoothing, filling and edge detection. The definition of circularity adopted here is: $C=4\pi\times A/P^2$, where A and P represent the area and perimeter of the selected contour, respectively. Obviously, the C value closer to unity indicates that the geometrical shape of the corresponding contour is closer to an ideal circle. Fig.5 presents the circularity characterizations of the micro-tubes with identifying numbers in Fig. 4 (a) and (d). The average circularities of the outer rings before and after the correction are 0.919 and 0.893, accompanying with those of the corresponding inner rings, 0.956 and 0.939, respectively. It is worth noting that compared with the inner rings, the outer rings are more sensitive to the aberration in our setup.

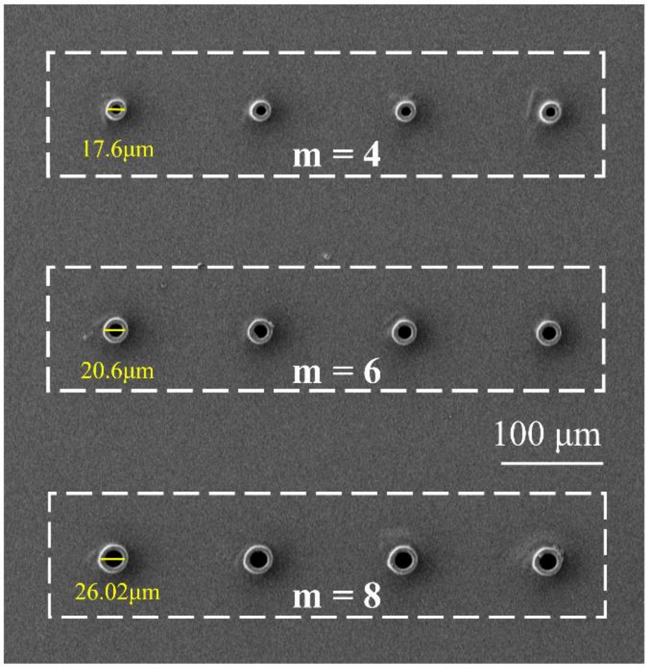

Fig. 6. SEM photo of micro-tubes fabricated with high-order Bessel beams of different vortex charges.

It is widely known that the vortex charge m can also affect the size of the main intensity lobe. To demonstrate the validity of this approach, we also fabricate micro-tubes with Bessel beams of different vortex charges. In the fabrication, the laser power and the exposure time are adapted accordingly due to the change of the lobe size. Fig.6 presents the SEM images of micro-tubes fabricated by high-order Bessel beams with vortex charges of 4, 6, and 8, and the measured outer rings diameters are 17.6 μm, 20.6 μm and 26.06 μm, respectively. All of the micro-tube structures present high-quality roundness and robust attachment to the substrate.

4. Conclusion

In this paper, we have demonstrated the powerful feasibility of the multi-channel interference wave-front sensing in adaptive-optics-based two-photon polymerization. To demonstrate this, significant aberrations are intentionally introduced in the installation of our homebuilt system for ultrafast laser processing without great efforts. Without additional wave-front sensor, more than 4π wave-front fluctuation across the input beam can be well flattened with the integration of the above wave-front sensing scheme. This results in significant improvement of fabrication quality with corrected high-order Bessel beams. Since the integration of this wave-front sensing technique requires no knowledge on the advanced mathematical skills for workers, such as Zernike-polynomial-based decomposition, Gerchberg-Saxton iteration and/or more complex algorithms, this straightforward solution would be highly attractive to implement in the laser processing system based on adaptive optics. Besides, our work also shows a promising perspective on significantly lowering the cost of the fabricating system by sparing the ultrafast lasers with super high-quality beams and exhausting alignments. We envision that our work will be very attractive in a broader scope of laser processing, where a well-defined wave-front is desired, such as the femtosecond laser-induced periodic surface structures [42]. For present, the wave-front correction is performed just before the fabrication without any real-time feedback during the printing process. But we also notice that a novel monitoring method would allow real-time monitoring the printing [43]. We remark that this method together with our technique would be a good solution to correcting not only the aberration from the optical system but also the distortions from other factors in the fabricating process. Future works may also be contributed to the fine feature correction with the complex amplitude modulation.

Funding Sources. This work was supported by the National Natural Science Foundation of China (62275191, 61605142, 61827821); Tianjin Research Program of Application Foundation and Advanced Technology of China (17JCJQJC43500); Shanghai Institute of Optics and Fine Mechanics, Chinese Academy of Sciences (Open Fund of the State Key Laboratory of High Field Laser Physics); European Research Council (682032-PULSAR); Agence Nationale de la Recherche (ANR-15-IDEX-0003, ANR-17-EURE-0002).

References

1. S. Kawata, H. Sun, T. Tanaka and K. Takada, "Finer features for functional microdevices," Nature 412(6848), 697-698 (2001).
2. L. Jiang, W. Xiong, Y. Zhou, Y. Liu, X. Huang, D. Li, T. Baldacchini, L. Jiang and Y. Lu, "Performance comparison of acrylic and thiol-acrylic resins in two-photon polymerization," Opt. Express 24(12), 13687 (2016).
3. W. Chu, Y. Tan, P. Wang, J. Xu, W. Li, J. Qi and Y. Cheng, "Centimeter-Height 3D Printing with Femtosecond Laser Two-Photon Polymerization," Advanced Materials Technologies 3, 1700396 (2018).

4. L. Li, R. Gattass, E. Gershgoren, H. Hwang and J. Fourkas, "Achieving λ /20 Resolution by One-Color Initiation and Deactivation of Polymerization," Science 324, 910-913 (2009).
5. T. Frenzel, M. Kadic and M. Wegener, "Three-dimensional mechanical metamaterials with a twist," Science 358, 1072-1074 (2017).
6. A. Bogucki, Ł. Zinkiewicz, M. Grzeszczyk, W. Pacuski, K. Nogajewski, T. Kazimierczuk, A. Rodek, J. Suffczyński, K. Watanabe, T. Taniguchi, P. Wasylczyk, M. Potemski and P. Kossacki, "Ultra-long-working-distance spectroscopy of single nanostructures with aspherical solid immersion microlenses," Light: Science & Applications 9, 48 (2020).
7. P. Dietrich, G. Göring, M. Trappen, M. Blaicher, W. Freude, T. Schimmel, H. Hölscher and C. Koos, "3D - Printed Scanning - Probe Microscopes with Integrated Optical Actuation and Read - Out," Small 16, 1904695 (2019).
8. C. Wang, L. Yang, C. Zhang, S. Rao, Y. Wang, S. Wu, J. Li, Y. Hu, D. Wu, J. Chu and K. Sugioka, "Multilayered skyscraper microchips fabricated by hybrid "all-in-one" femtosecond laser processing," Microsystems & Nanoengineering 5, 17 (2019).
9. Z. Ma, Y. Zhang, B. Han, X. Hu, C. Li, Q. Chen and H. Sun, "Femtosecond laser programmed artificial musculoskeletal systems," Nat. Commun. 11, 4536 (2020).
10. P. S. Salter, and M. J. Booth, "Adaptive optics in laser processing," Light Sci. Appl. 8, 110 (2019).
11. S. Gittard, A. Nguyen, K. Obata, A. Koroleva, R. Narayan and B. Chichkov, "Fabrication of microscale medical devices by two-photon polymerization with multiple foci via a spatial light modulator," Biomed. Opt. Express 2, 3167 (2011).
12. X. Li, Y. Cao, N. Tian, L. Fu and M. Gu, "Multifocal optical nanoscopy for big data recording at 30 TB capacity and gigabits/second data rate," Optica 2, 567-570 (2015).
13. P. Salter and M. Booth, "Dynamic control of directional asymmetry observed in ultrafast laser direct writing," Appl. Phys. Lett. 101, 141109 (2012).
14. L. Yang, A. El-Tamer, U. Hinze, J. Li, Y. Hu, W. Huang, J. Chu and B. Chichkov, "Two-photon polymerization of cylinder microstructures by femtosecond Bessel beams," Applied Physics Letters 105, 041110 (2014).
15. B. Mills, D. Kundys, M. Farsari, S. Mailis, and R. W. Eason, "Single-pulse multiphoton fabrication of high aspect ratio structures with sub-micron features using vortex beams," Appl. Phys. A 108, 651-655 (2012).
16. E. Stankevicius, T. Gertus, M. Rutkauskas, M. Gedvilas, G. Raciukaitis, R. Gadonas, V. Smilgevicius, and M. Malinauskas, "Fabrication of micro-tube arrays in photopolymer SZ2080 by using three different methods of a direct laser polymerization technique," Journal of Micromechanics and Microengineering 22, 065022 (2012).
17. L. Yang, D. Qian, C. Xin, Z. Hu, S. Ji, D. Wu, Y. Hu, J. Li, W. Huang and J. Chu, "Direct laser writing of complex microtubes using femtosecond vortex beams," Applied Physics Letters 110, 221103 (2017).
18. M. Manousidaki, D. Papazoglou, M. Farsari and S. Tzortzakis, "Abruptly autofocusing beams enable advanced multiscale photo-polymerization," Optica 3, 525-530 (2016).
19. D. Pan, S. Liu, S. Ji, Z. Cai, J. Li, Y. Hou, W. Zhang, S. Fan, R. Li, Y. Hu, W. Zhu, D. Wu and J. Chu, "Efficient fabrication of a high-aspect-ratio AFM tip by one-step exposure of a long focal depth holographic femtosecond axilens beam," Opt. Lett. 45, 897-900 (2020).
20. D. Yang, L. Liu, Q. Gong, and Y. Li, "Rapid Two-Photon Polymerization of an Arbitrary 3D Microstructure with 3D Focal Field Engineering," Macromol. Rapid Comm. 40, 1900041 (2019).
21. G. Kontenis, D. Gailevičius, N. Jiménez, and K. Staliunas, "Optical Drills by Dynamic High-Order Bessel Beam Mixing," Phys. Rev. Appl. 17, 034059 (2022).
22. V. Anand, S. Khonina, R. Kumar, N. Dubey, A. N. K. Reddy, J. Rosen, and S. Juodkazis, "Three-Dimensional Incoherent Imaging Using Spiral Rotating Point Spread Functions Created by Double-Helix Beams [Invited]," Nanoscale Res. Lett. 17, 37 (2022).
23. B. Wetzel, C. Xie, P. Lacourt, J. M. Dudley, and F. Courvoisier, "Femtosecond laser fabrication of micro and nano-disks in single layer graphene using vortex Bessel beams," Appl. Phys. Lett. 103, 241111 (2013).
24. W. Yu, Z. Ji, D. Dong, X. Yang, Y. Xiao, Q. Gong, P. Xi, and K. Shi, "Super-resolution deep imaging with hollow Bessel beam STED microscopy," Laser Photonics Rev. 10, 147-152 (2016).
25. K. Volke-Sepulveda, V. Garcés-Chávez, S. Chávez-Cerda, J. Arlt, and K. Dholakia, " Orbital angular momentum of a high-order Bessel light beam," J. Opt. B 4, S82 (2002).
26. H. Zhang, W. Ding, P. Fu, X. Liu, Y. Gao, Y. Gao, Y. Cai, and Y. Yuan, "Reducing orbital angular momentum crosstalk of the Bessel-Gaussian beam for underwater optical communications," Journal of Optics 22, 65702 (2020).
27. Y. Yuan, T. Lei, Z. Li, Y. Li, S. Gao, Z. Xie, and X. Yuan, "Beam wander relieved orbital angular momentum communication in turbulent atmosphere using Bessel beams," Sci. Rep. 7, 42276(2017).
28. B. Miao, L. Feder, J. E. Shrock, and H. M. Milchberg, "Phase front retrieval and correction of Bessel beams," Opt. Express 30, 11360-11371 (2022).
29. K. Wulff, D. Cole, R. Clark, R. DiLeonardo, J. Leach, J. Cooper, G. Gibson, and M. Padgett , "Aberration correction in holographic optical tweezers," Opt. Express 14, 4169–4174 (2006).
30. A. Jesacher, A. Schwaighofer, S. Fürhapter, C. Maurer, S. Bernet, and M. Ritsch-Marte, "Wavefront correction of spatial light modulators using an optical vortex image," Opt. Express 15, 5801-5808 (2007).
31. Y. Liang, Y. Cai, Z. Wang, M. Lei, Z. Cao, Y. Wang, M. Li, S. Yan, P. R. Bianco, and B. Yao, "Aberration correction in holographic optical tweezers using a high-order optical vortex," Appl. Opt. 57, 3618 (2018).
32. D. Armstrong, A. Stilgoe, T. Nieminen, and H. Rubinsztein-Dunlop, "Improved two-photon photopolymerisation and optical trapping with aberration-corrected structured light," Front. Nanotechnol. 4, 998656 (2022).
33. N. Sanner, N. Huot, E. Audouard, C. Larat, J.-P. Huignard, and B. Loiseaux, "Programmable focal spot shaping of amplified femtosecond laser pulses," Opt. Lett. 30, 1479-1481 (2005).
34. C. Mauclair, A. Mermillod-Blondin, N. Huot, E. Audouard, and R. Stoian, "Ultrafast laser writing of homogeneous longitudinal waveguides in glasses using dynamic wavefront correction," Opt. Express 16, 5481-5492 (2008).
35. C. Xie, V. Jukna, C. Milian, R. Giust, I. Ouadghiri-Idrissi, T. Itina, J. M. Dudley, A. Couairon, and F. Courvoisier, "Tubular filamentation for laser material processing," Sci. Rep. 5, 8914 (2015).

36. T. Čižmár, M. Mazilu, and K. Dholakia, "In situ wavefront correction and its application to micromanipulation," Nat. Photonics 4, 388-394 (2010).
37. H. Song, B. Liu, Y. Li, Y. Song, H. He, L. Chai, M. Hu, and C. Wang, "Practical 24-fs, 1-μJ, 1-MHz Yb-fiber laser amplification system," Opt. Express 25, 7559-7566 (2017).
38. C. Xie, R. Giust, V. Jukna, L. Furfaro, M. Jacquot, P. Lacourt, L. Froehly, J. Dudley, A. Couairon, and F. Courvoisier, "Light trajectory in Bessel-Gauss vortex beams," J. Opt. Soc. Am. A 32, 1313-1316 (2015)
39. H. Zhang, J. Xie, J. Liu, and Y. Wang, "Elimination of a zero-order beam induced by a pixelated spatial light modulator for holographic projection," Appl. Opt. 48, 5834 (2009).
40. N. Xiao, C. Xie, E. Jia, J Li, R. Giust, F. Courvoisier, and M. Hu, "Caustic Interpretation of the Abruptly Autofocusing Vortex beams", Opt. Express 29, 19975–19984 (2021).
41. A. Ovsianikov, X. Shizhou, M. Farsari, M. Vamvakaki, C. Fotakis, and B. N. Chichkov, "Shrinkage of microstructures produced by two-photon polymerization of Zr-based hybrid photosensitive materials," Opt. Express 17, 2143-2148 (2009).
42. J. Geng, X. Fang, L. Zhang, G. Yao, L. Xu, F. Liu, W. Tang, L. Shi, and M. Qiu, "Controllable generation of large-scale highly regular gratings on Si films," Light: Advanced Manufacturing 2, 281 (2021).
43. R. Zvagelsky, F. Mayer, D. Beutel, C. Rockstuhl, G. Gomard, and M. Wegener, "Towards in-situ diagnostics of multi-photon 3D laser printing using optical coherence tomography," Light: Advanced Manufacturing 3, 466-480 (2021).